

Atomic structure of the PL5 defect in silicon carbide revealed by single-spin spectroscopy and oxygen implantation

Yu Chen,^{1,2,*} Qi Zhang*,^{1,3,4,†} Mingzhe Liu,^{1,*} Junda Wu,^{1,3,*} Jinpeng Liu,^{1,3} Xin Zhao,¹ Jingyang Zhou,¹ Pei Yu,¹ Shaochun Lin,¹ Yuanhong Teng,¹ Wancheng Yu,⁵ Ya Wang,^{1,2,6} Chang-Kui Duan,^{1,2,6} and Fazhan Shi^{1,2,3,6,‡}

¹Laboratory of Spin Magnetic Resonance, School of Physical Sciences,
and Anhui Province Key Laboratory of Scientific Instrument Development and Application,
University of Science and Technology of China, Hefei 230026, China

²Hefei National Laboratory, University of Science and Technology of China, Hefei 230088, China

³School of Biomedical Engineering and Suzhou Institute for Advanced Research,
University of Science and Technology of China, Suzhou 215123, China

⁴Institute of Quantum Sensing, School of Physics,
Institute of Fundamental and Transdisciplinary Research,
Zhejiang Key Laboratory of R&D and Application of Cutting-edge
Scientific Instruments, Zhejiang University, Hangzhou, 310027, China

⁵State Key Laboratory of Crystal Materials, Institute of Novel Semiconductors, Shandong University, Jinan 250100, China

⁶Hefei National Research Center for Physical Sciences at the Microscale,
University of Science and Technology of China, Hefei 230026, China

PL5 and PL6 centers in 4H-SiC are promising for quantum applications due to their superior charge stability and optically detected magnetic resonance (ODMR) properties at room temperature. However, their atomic structures remain unresolved, with ongoing controversy regarding their potential association with stacking faults. Previous measurements relying on spin ensemble detection were insufficient to draw definitive conclusions. In this work, we conduct correlative imaging of stacking faults and PL5/PL6 at the single-defect level, definitively ruling out any spatial correlation and demonstrating that these centers are not associated with stacking faults. Furthermore, we find that substituting oxygen for nitrogen in ion implantation enhances the yields of PL5 and PL6 by more than 11-fold and 23-fold, respectively. Single-spin ODMR spectroscopy of PL5 reveals six distinct orientations, determines the transverse zero-field splitting parameter E , and characterizes the hyperfine coupling. Combined with our *ab initio* calculations, these results provide compelling evidence for the assignment of PL5 as an OV(kh) defect, consisting of an oxygen atom occupying the C(k) site as the nearest neighbor to a Si(h) vacancy. The structural analysis together with the demonstrated defect yield enhancement lays the foundation for fabricating high-sensitivity, high-contrast ensemble quantum sensors in two and three dimensions.

INTRODUCTION

The properties of electronic spins in semiconductors are pivotal in their applications in quantum sensing and quantum networks. A thorough understanding of these properties necessitates detailed insights into their atomic structures [1]. Divacancy-related spin defects in 4H-SiC exhibit long coherence times and emission at near telecommunication wavelengths [2–5]. Recent advancements have showcased their integration into p-i-n structures [6], photonic waveguide [7] and photonic crystal cavities [8, 9], demonstrating their potential compatibility with scalable industrial nanofabrication. While four of these defects in 4H-SiC, named PL1–4, have been confirmed as divacancies ($V_{\text{Si}}V_{\text{C}}$) [5, 10], other color centers, PL5–8, have been found to exhibit properties similar to those of PL1–4 and are considered as divacancy perturbed by the presence of other defects [5, 11, 12]. Among them, PL5–6 exhibit remarkably high charge stability and ODMR contrast at room temperature, in contrast to PL1–4 [11, 13–17]. Their spin properties are highly comparable to those of the widely studied nitrogen-vacancy (NV) center in diamond, while their application can fur-

ther benefit from infrared emission and CMOS compatibility [14, 18]. Notably, we observe high fluorescence rates of 460 kcps (kilo counts per second) for single PL6 and 250 kcps for single PL5 (Fig. S1 in [19]) without any photonic structure enhancement, highlighting their competitiveness as quantum sensors compared to the NV center in diamond. Therefore, a detailed investigation into the atomic structure of PL5–6 is essential, as it holds the key to understanding their properties and facilitating their controllable generation.

A previously widely accepted model suggested that PL5–6 are likely divacancies formed near stacking faults (VV-SF model) [20–24]. This model posits that the band gap narrowing effect caused by stacking faults is responsible for the high charge stability of PL5–6 [20]. However, direct experimental verification has been elusive; studies relying on ensemble-averaged detection have produced inconclusive or conflicting results due to limited spatial resolution [20, 25–28], necessitating more precise evidence to validate this hypothesis. More recently, an alternative model proposed identifying PL5 and PL6 as neutral oxygen-substituted silicon vacancies ($O_{\text{C}}V_{\text{Si}}$) [29]. While this inspiring proposal was initially supported by comparisons of the zero-field splitting parameter D ,

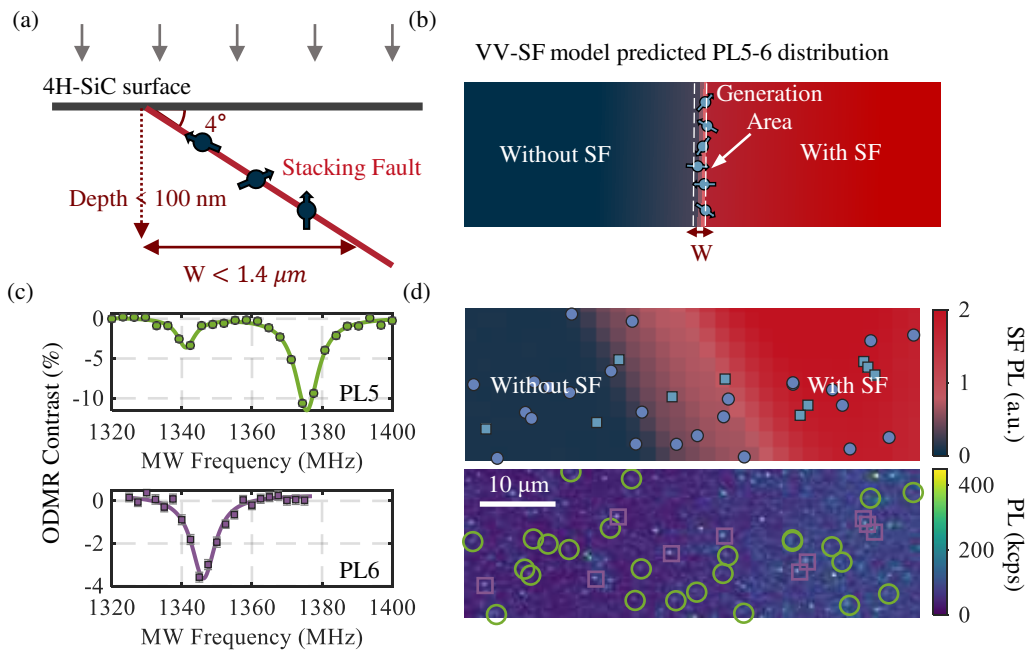


FIG. 1. (a) Schematic illustration of the VV-SF model. (b) Predicted distribution of PL5-6 color centers based on the VV-SF model. (c) ODMR spectra of PL5 and PL6 measured in the sample. (d) Confocal images of the stacking fault edge region: the top image displays the integrated photoluminescence intensity from 410-430 nm under 325 nm laser excitation, while the bottom image shows the photoluminescence intensity of PL5 and PL6 under 914 nm laser excitation in the same area. Circles denote the locations of PL5, and squares indicate the locations of PL6.

zero-phonon lines (ZPL), and radiative lifetimes, these parameters alone are not unique fingerprints for structural identification. As discussed in the Supplementary Material [19], other complex structures—such as divacancies perturbed by antisites—can also satisfy these screening criteria. In this work, we systematically examine these models based on single-defect imaging and single-spin spectroscopy. First, we address the VV-SF hypothesis by performing correlative single-defect-level imaging of stacking faults and PL5-6 centers. Our results demonstrate that PL5-6 can form far from stacking faults, definitively ruling out the VV-SF model. Subsequently, to test the $O_C V_{Si}$ model, we substitute standard nitrogen implantation with oxygen implantation. We observe a dramatic enhancement in generation efficiency, with PL5 and PL6 yields increasing by factors higher than 11 and 23, respectively, providing compelling evidence for the presence of oxygen in these defects. Finally, to determine the specific atomic configuration, we employ single-spin ODMR spectroscopy to resolve the precise orientations of the zero-field splitting tensors (D , E) and characterize the hyperfine couplings with nearby nuclear spins. Through a detailed comparison of these rigorous experimental constraints with *ab initio* calculations, we find that our experimental data are best matched by the $O_C V_{Si}$ defect model in the kh configuration, rather than the previously proposed hk assignment [29].

TEST OF VV-SF MODEL

The sample was diced from a wafer consisting of a 12.5- μm -thick intrinsic epitaxial layer of single-crystal 4H-SiC grown on a 4° off-axis N-type 4H-SiC substrate. To generate PL5-6, 15-keV $^{14}\text{N}^+$ ions were implanted at a dose of approximately 10^{11} cm^{-2} , followed by annealing at 1000°C for 30 minutes. According to the VV-SF model, PL5-6 should be generated near the stacking fault, and the ion implantation depth further restricts the PL5-6 to be shallower than 100 nm [30]. As the SF is inclined at an angle of 4° to the sample surface in our sample, PL5-6 should be distributed along the intersection line between the SF and the surface, within an area approximately $1.4\mu\text{m}$ wide, as illustrated in Fig. 1(a-b).

To test the VV-SF model, we mapped the location of PL5-6 using single-spin ODMR. The ODMR spectra of PL5-6 in our sample are shown in Fig. 1(c) and Fig. S2 [19]. We then mapped the SF in the same region using the PL method described in [31]. The intrinsic 4H-SiC PL spectrum exhibits a band-edge emission peak at 386 nm (3.21 eV) when illuminated by a 325 nm laser. The SF lowers the bandgap, causing a redshift in the PL spectrum [20, 31], allowing its detection with the PL method. We collected PL spectra ranging from 400 nm to 520 nm in a $180\mu\text{m} \times 180\mu\text{m}$ region. Only 420 nm (2.95 eV) PL peaks corresponding to two SF types, single Shockley SFs and intrinsic Frank SFs [31], were observed in this region (Fig. S3 in [19]). This bandgap lowering of 0.26 eV is consistent with the calculation in [20] and

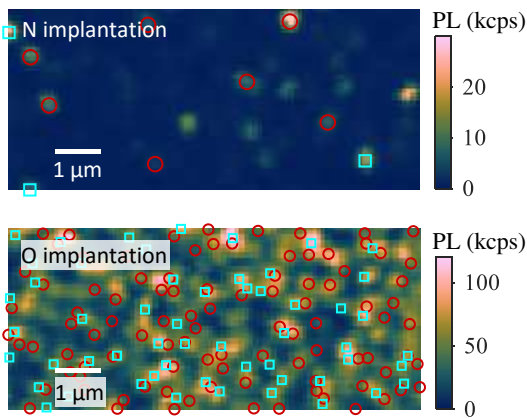


FIG. 2. (a) Photoluminescence (PL) image of a nitrogen-implanted sample. Implantation was performed at 15 keV with a dose of 10^{11} cm^{-2} , followed by annealing at 1050°C for 30 minutes. (b) PL image of an oxygen-implanted sample under identical implantation and annealing conditions. In both panels, PL5 and PL6 centers identified by ODMR (see Supplementary Material [19]) are marked with blue squares and red circles, respectively.

has been used to interpret the charge stability of PL5–6. Fig. 1(d) shows an area of the sample with an SF edge. The SF PL at each point is given by the integral of PL intensity from 410–430 nm. Contrary to the VV-SF model’s prediction, we observed PL5–6 far from the stacking fault edge, indicating that the VV-SF model does not hold for PL5–6.

TEST OF OV MODEL

To test the oxygen vacancy (OV) model, we compare the results from oxygen-implanted samples with those implanted with nitrogen ions. The concentration of oxygen in as-grown 4H-SiC CVD epilayers is typically low ($<10^{12} \text{ cm}^{-3}$) [32, 33]. Therefore, oxygen implantation can substantially increase the oxygen density. If PL5/6 is indeed related to an OV complex, its production efficiency should increase dramatically upon oxygen implantation. Fig. 2 presents photoluminescence (PL) mapping results for samples implanted with oxygen and nitrogen at the same dose and energy (15 keV, 10^{11} cm^{-2} , followed by annealing at 1050°C for 30 minutes). The overall PL intensity of the oxygen-implanted sample is brighter than that of the nitrogen-implanted one. Using optically detected magnetic resonance (see Supplementary Material [19]), we identified individual emission spots corresponding to PL5 and PL6 centers. These are marked with circles (PL5) and squares (PL6) in Fig. 2. Statistical analysis over a larger area (Supplementary Material [19]) reveals that the generation efficiency of PL5 and PL6 centers in the oxygen-implanted sample is at least 11 and 23 times higher, respectively, than in the nitrogen-implanted sample. The order-of-magnitude enhancement in PL5/6 generation upon oxygen implanta-

tion illustrates that oxygen plays an important role in PL5 generation and increases the reliability of OV model.

Therefore, focusing on PL5, we perform additional measurements on the color centers ground-state spin Hamiltonian for comparison with $\text{O}_\text{C}\text{V}_{\text{Si}}$ *ab initio* calculations. Previous experimental studies have deter-

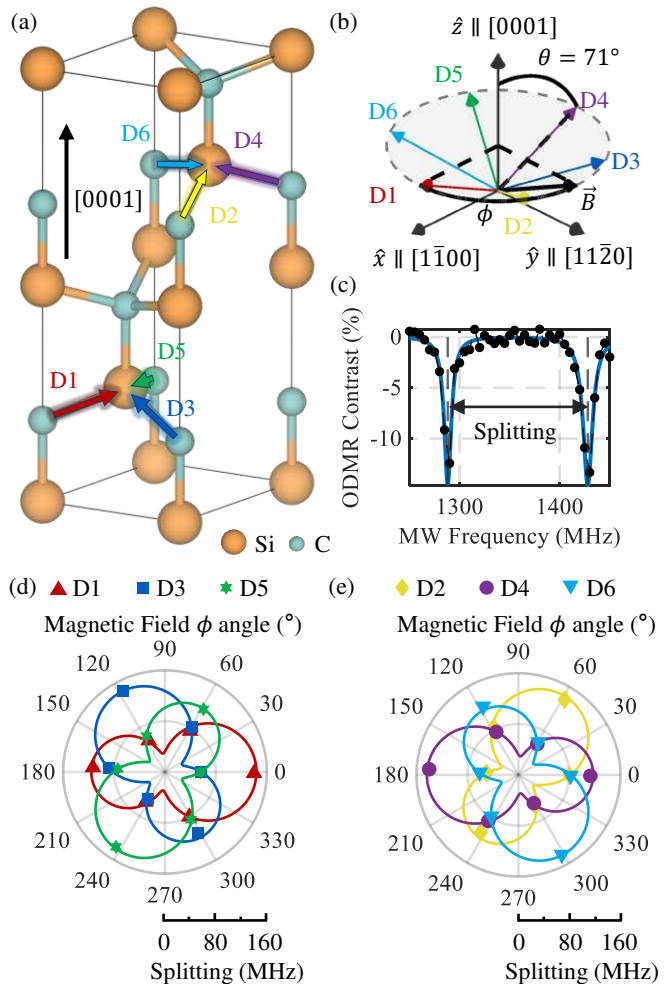


FIG. 3. (a) Schematic of six PL5 directions D1–D6 in 4H-SiC lattice. (b) Schematic of six PL5 directions, coordinate axes, and the magnetic field for measurements in (d–e). The magnitude of the magnetic field was set to 25 Gauss. (c) ODMR spectrum of a D1 direction PL5 under $\phi = 30^\circ$. (d)(e) Polar plots of ODMR splittings of PL5 of different orientations as functions of the magnetic orientation ϕ .

mined the PL5 axially symmetric spin splitting as $D = 1360 \text{ MHz}$ and transverse anisotropy splitting as $E = 16 \text{ MHz}$ [11, 14] at room temperature. Here, we further resolve their orientations, which are important as they are correlated with atomic structures. We found that PL5 are equally distributed among the six orientations of the basal C-Si bonds in 4H-SiC [Fig. 3(a)]. This observation is well supported by the results of rotational magnetic field experiments. By rotating the magnetic field on a conical surface at a 71° angle to the c-axis and measuring the splitting of PL5 centers [Fig. 3(b–c)], we found there are six types of rotating angle dependence

as depicted in Fig. 3(d–e). Each dependence corresponds to one direction of PL5, revealing there are six directions (D1–D6) of PL5. It should be noted that PL3–5 centers, as basal divacancies, are all expected to have six orientations. Previous reports observed three orientations of basal divacancies, mostly because the applied fields (microwave, strain, and excitation laser) were confined within the c -plane in those studies [5, 14, 34].

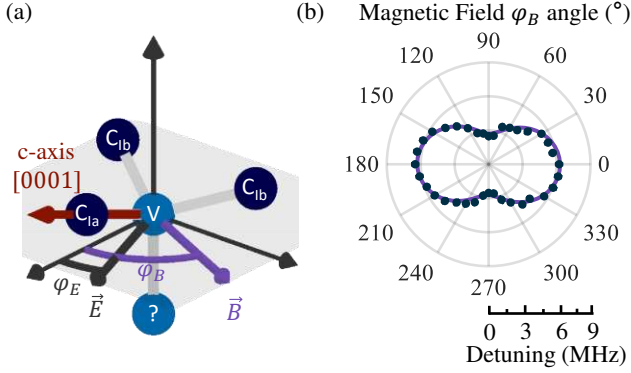


FIG. 4. (a) Schematic of PL5, coordinate axes and the magnetic field. The magnitude of the magnetic field was set to 25 Gauss. The coordinate axes are defined such that the direction of axially symmetric splitting is selected as the z -axis. The coordinate system is chosen such that the c -axis lies within the xz plane. (b) Polar plot of the measured detuning as a function of the magnetic orientation φ_B . The detuning is set from $f_0 = 1375.3$ MHz. Fitting using Eq. (1) yields $\varphi_E = 182.2 \pm 3.5^\circ$.

The coordinate system for measuring the direction of E is defined such that the direction of D align with the z -axis, while the crystal c -axis lies within the xz plane [Fig. 4(a)]. We applied a magnetic field of 25 Gauss rotating around the z -axis to measure the azimuth angle φ_E of E [35]. The two magnetic dipole transition frequencies measured on the ODMR spectrum of PL5 are given by [35, 36]

$$f_{\pm} = D + 3\eta \pm (E^2 - 2\eta \cos(2\varphi_B + \varphi_E) + \eta^2)^{\frac{1}{2}} \quad (1)$$

where φ_B is the azimuth angle of magnetic field B and $\eta = (\gamma B)^2 / 2D$. Fig. 4(b) gives the experimentally measured f_+ as a function of φ_B , and fitting with Eq. (1) yields $\varphi_E = 182.2 \pm 3.5^\circ$, indicating that the direction of E is in the symmetry plane of divacancy.

The carbon atoms adjacent to the V_{Si} in PL5, denoted as C_{1a} and C_{1b} in Fig. 4(a), exhibit the strongest hyperfine coupling with PL5. To quantify this coupling, we measured the ODMR spectra of PL5 coupled with a $^{13}C_{1a}$ ($^{13}C_{1b}$) nuclear spin under an aligned magnetic field [Fig. 5(a)]. We observed slight differences between the hyperfine splittings of the $|0\rangle \leftrightarrow |+1\rangle$ and $|0\rangle \leftrightarrow |-1\rangle$ transitions (Table S4). The mean value of these splittings is defined as the characteristic hyperfine splitting δ . Measurements of δ were performed for three PL5 centers coupled with $^{13}C_{1a}$ and four with $^{13}C_{1b}$ [Fig. 5(b)]. The $^{13}C_{1a}$ -coupled centers exhibited systematically larger

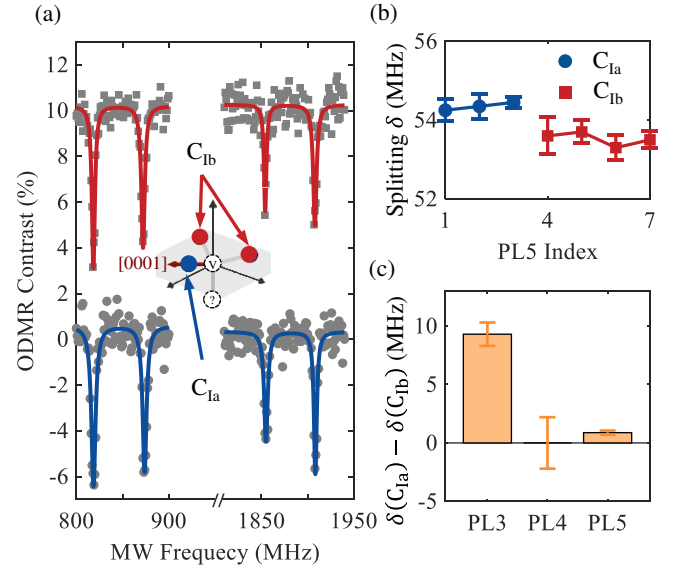


FIG. 5. (a) ODMR spectra of PL5 coupled to a $^{13}C_I$ nuclear spin adjacent to the V_{Si} in PL5. Blue (Red) line represents the fit to the data of PL5 coupled with $^{13}C_{1a}$ ($^{13}C_{1b}$). All spectra were acquired under an applied magnetic field of 185 Gauss. (b) Hyperfine splitting δ induced by the interaction with $^{13}C_{1a}$ (blue) and $^{13}C_{1b}$ (red), as derived from different PL5. (c) The splitting difference $\delta(C_{1a}) - \delta(C_{1b})$ for PL3–5. Experimental data for PL3 and PL4 are reproduced from [10].

splittings by 0.88 MHz compared to their $^{13}C_{1b}$ counterparts.

Accurate determination of the orientations of D , E , and the hyperfine splitting difference $\delta(C_{1a}) - \delta(C_{1b})$ enables direct comparison with theoretical predictions of various atomic structure models. Here, we performed first-principles calculations on neutral oxygen-substituted silicon vacancies and divacancies based on density functional theory (DFT) to describe the electronic structure and spin properties of candidate systems. The electronic calculations for 4H-SiC were performed using the Vienna ab initio simulation package (VASP) [37, 38] with the projector augmented wave method [39]. To balance accuracy and computational cost, these systems are simulated in a 478-atom supercell with PBEsol density functional [40], 520 eV energy cutoff and Γ point sampling. The lattice of the supercell is orthogonal, whose parameters are given as 16.07, 15.48, and 20.25 Å. To ensure a robust search for the defect ground state, small random perturbations were applied to the initial atomic coordinates without enforcing symmetry constraints during relaxation. Consequently, the optimized structures and electronic properties may exhibit minor deviations from ideal symmetry.

The ZPL and charge transition levels are estimated by the single electronic orbitals at the equilibrium structures of the spin-triplet states. The zero-field splitting is calculated using a formalism that employs Kohn-Sham orbitals obtained from periodic density functional calculations [41]. The hyperfine tensors for nuclei are cal-

TABLE I: Comparison of selected *ab initio* calculation results with experimental properties of PL3–5. Experimental values for ZPL, D , and E at low temperature are reported in [11, 34]. For PL5, $E_x = E \cos \varphi_E$ and $E_y = E \sin \varphi_E$, where φ_E is measured in this paper. $\delta(C_{1a})$ and $\delta(C_{1b})$ are hyperfine splittings due to the nearest ^{13}C nuclei C_{1a} and C_{1b} . The experimental splitting differences $\delta(C_{1a}) - \delta(C_{1b})$ for PL3–5 are obtained from Fig. 5.

Label	ZPL (eV)	D (MHz)	E_x (MHz)	$ E_y $ (MHz)	$\delta(C_{1a}) - \delta(C_{1b})$ (MHz)
(Exp.) PL5	1.189	1373	-16.5	<0.5	0.88
(Cal.) $\text{O}_\text{C}\text{V}_{\text{Si}}(kh)$	1.12	1552	-47.0	7.7	0.89
(Cal.) $\text{O}_\text{C}\text{V}_{\text{Si}}(hk)$	1.06	1440	-96.5	-7.8	2.32
(Exp.) PL4	1.118	1334	$\sqrt{E_x^2 + E_y^2} = 18.7$		<3
(Cal.) $\text{V}_\text{C}\text{V}_{\text{Si}}(kh)$	1.12	1465	-33.9	0.0	1.72
(Exp.) PL3	1.119	1222	$\sqrt{E_x^2 + E_y^2} = 82$		9.3
(Cal.) $\text{V}_\text{C}\text{V}_{\text{Si}}(hk)$	1.08	1402	-63.9	0.0	4.57

culated with VASP, taking into account the core electronic contributions using the frozen valence approximation [42]. We also perform calculations without core-polarization corrections and discuss their impact in the Supplementary Material [19]. The nuclear gyromagnetic ratios for ^{29}Si and ^{13}C nuclei are -8.465 MHz/T and 10.705 MHz/T, respectively. To improve the description of hyperfine coupling, the HSE06 hybrid functional was employed [43].

The comparison of the calculation result of identified PL3(*hk*) and PL4(*kh*) divacancies with their experimental counterparts shows our calculated D are overestimated by no more than 200 MHz; the calculation error is about 30 MHz for E and about 0.05 eV for ZPL (Table I). Within these errors, the calculated properties of $\text{O}_\text{C}\text{V}_{\text{Si}}(kh)$ show consistency with experimental data of PL5 (Table I).

We further compared *ab initio* results of $\text{O}_\text{C}\text{V}_{\text{Si}}$ couplings to nuclear spins (^{29}Si , ^{13}C) other than the C_I site with experimental results (Fig. 6). The experimental results are measured in 128 PL5 color centers which exhibited strong coupling with single nuclear spin other than the C_I site. To better visualize these results, we broadened each experimental point as a Gaussian peak, using the value as the center and the error bar as the variance, then summed these peaks, as shown in Fig. 6(b). For comparison, the simulated hyperfine couplings for the $\text{O}_\text{C}\text{V}_{\text{Si}}(kh)$ and $\text{O}_\text{C}\text{V}_{\text{Si}}(hk)$ configuration are represented as red solid line and green dashed lines in Fig. 6(b). The *ab initio* results of $\text{O}_\text{C}\text{V}_{\text{Si}}(kh)$ reasonably reproduce the hyperfine coupling parameters.

In summary, we have unambiguously ruled out the previously hypothesized VV-SF model through single-defect co-localization imaging. Our combined experimental and theoretical analysis provides compelling evidence identifying the PL5 center in 4H-SiC as the neutral oxygen-substituted silicon vacancy $\text{O}_\text{C}\text{V}_{\text{Si}}$ in the *kh* configuration. However, a conclusive final verification should be

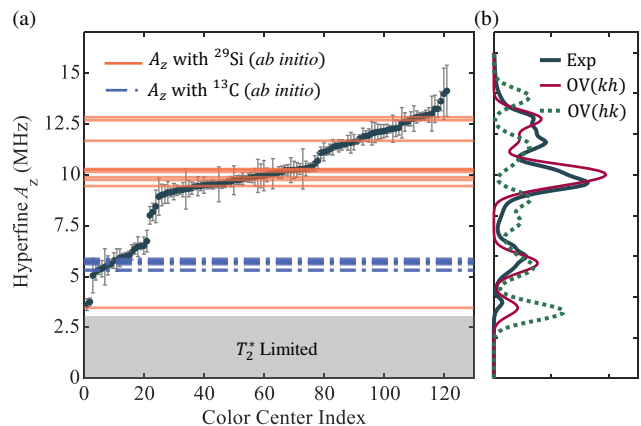


FIG. 6. (a) Measured hyperfine constant A_z for different color centers under an applied magnetic field of $\gamma B_z = 39.6 \pm 1$ MHz [19]. The color centers are sorted by A_z for clarity. Solid (dashed) lines represent $\text{O}_\text{C}\text{V}_{\text{Si}}(kh)$ ($ab initio$) results of couplings to ^{29}Si (^{13}C) spins at different lattice locations. The hyperfine couplings less than 3 MHz cannot be detected due to the ODMR broadening with T_2^* , marked by the shadow area. (b) Experimental (black solid curve) versus simulated $\text{O}_\text{C}\text{V}_{\text{Si}}(kh)$ (red solid curve) and $\text{O}_\text{C}\text{V}_{\text{Si}}(hk)$ (green dashed curve) A_z distributions. The experimental A_z distribution is generated by Gaussian broadening by broadening each data point in (b) as a Gaussian peak and then summing. The error bar of each point serves as the standard deviation for each experimental Gaussian peak. The simulated A_z distribution is given by the $\text{O}_\text{C}\text{V}_{\text{Si}}(kh)$ and $\text{O}_\text{C}\text{V}_{\text{Si}}(hk)$ *ab initio* results, with broadening of the average of the experimental error bars.

achieved by directly resolving the hyperfine interaction with the oxygen atom with ^{17}O -enriched samples. Nevertheless, the established role of oxygen and the yield enhancement via its implantation already provide a clear pathway for the deterministic, high-yield generation of these defects, which is crucial for scaling up quantum device fabrication.

This work was supported by the National Natural Science Foundation of China (Grant Nos. T2125011, 12174377), the CAS (Grant No. YSBR-068), Quantum Science and Technology-National Science and Technology Major Project (Grant Nos. 2021ZD0302200,

2021ZD0303204), New Cornerstone Science Foundation through the XPLOER PRIZE, "Pioneer" and "Leading Goose" R&D Program of Zhejiang (Grant No. 2025C01041) and the Fundamental Research Funds for the Central Universities (Grant No. 226-2024-00142). This work was partially carried out at the USTC Center for Micro and Nanoscale Research and Fabrication. The numerical calculations were performed on the supercomputing system at the Supercomputing Center of the University of Science and Technology of China.

* These authors contributed equally to this work.

† zhq2011@ustc.edu.cn; These authors contributed equally to this work.

‡ fzshi@ustc.edu.cn

- [1] G. Wolfowicz, F. J. Heremans, C. P. Anderson, S. Kanai, H. Seo, A. Gali, G. Galli, and D. D. Awschalom, Quantum guidelines for solid-state spin defects, *Nature Reviews Materials* **6**, 906 (2021).
- [2] C. P. Anderson, E. O. Glen, C. Zeledon, A. Bourassa, Y. Jin, Y. Zhu, C. Vorwerk, A. L. Crook, H. Abe, J. Ul-Hassan, T. Ohshima, N. T. Son, G. Galli, and D. D. Awschalom, Five-second coherence of a single spin with single-shot readout in silicon carbide, *Science Advances* **8**, eabm5912 (2022).
- [3] A. Bourassa, C. P. Anderson, K. C. Miao, M. Onizhuk, H. Ma, A. L. Crook, H. Abe, J. Ul-Hassan, T. Ohshima, N. T. Son, G. Galli, and D. D. Awschalom, Entanglement and control of single nuclear spins in isotopically engineered silicon carbide, *Nature Materials* **19**, 1319 (2020).
- [4] D. J. Christle, A. L. Falk, P. Andrich, P. V. Klimov, J. U. Hassan, N. T. Son, E. Jánzén, T. Ohshima, and D. D. Awschalom, Isolated electron spins in silicon carbide with millisecond coherence times, *Nature Materials* **14**, 160 (2015).
- [5] W. F. Koehl, B. B. Buckley, F. J. Heremans, G. Calusine, and D. D. Awschalom, Room temperature coherent control of defect spin qubits in silicon carbide, *Nature* **479**, 84 (2011).
- [6] C. P. Anderson, A. Bourassa, K. C. Miao, G. Wolfowicz, P. J. Mintun, A. L. Crook, H. Abe, J. Ul Hassan, N. T. Son, T. Ohshima, and D. D. Awschalom, Electrical and optical control of single spins integrated in scalable semiconductor devices, *Science* **366**, 1225 (2019).
- [7] H. Hu, Y. Zhou, A. Yi, T. Bao, C. Liu, Q. Luo, Y. Zhang, Z. Wang, Q. Li, D. Lu, Z. Liu, S. Xiao, X. Ou, and Q. Song, Room-temperature waveguide integrated quantum register in a semiconductor photonic platform, *Nature Communications* **15**, 10256 (2024).
- [8] G. Calusine, A. Politi, and D. D. Awschalom, Silicon carbide photonic crystal cavities with integrated color centers, *Applied Physics Letters* **105**, 011123 (2014).
- [9] A. L. Crook, C. P. Anderson, K. C. Miao, A. Bourassa, H. Lee, S. L. Bayliss, D. O. Bracher, X. Zhang, H. Abe, T. Ohshima, E. L. Hu, and D. D. Awschalom, Purcell Enhancement of a Single Silicon Carbide Color Center with Coherent Spin Control, *Nano Letters* **20**, 3427 (2020).
- [10] N. T. Son, P. Carlsson, J. ul Hassan, E. Jánzén, T. Umeda, J. Isoya, A. Gali, M. Bockstedte, N. Morishita, T. Ohshima, and H. Itoh, Divacancy in 4H-SiC, *Physical Review Letters* **96**, 055501 (2006).
- [11] A. L. Falk, B. B. Buckley, G. Calusine, W. F. Koehl, V. V. Dobrovitski, A. Politi, C. A. Zorman, P. X.-L. Feng, and D. D. Awschalom, Polytype control of spin qubits in silicon carbide, *Nature Communications* **4**, 1819 (2013).
- [12] F.-F. Yan, A.-L. Yi, J.-F. Wang, Q. Li, P. Yu, J.-X. Zhang, A. Gali, Y. Wang, J.-S. Xu, X. Ou, C.-F. Li, and G.-C. Guo, Room-temperature coherent control of implanted defect spins in silicon carbide, *npj Quantum Information* **6**, 1 (2020).
- [13] G. Wolfowicz, C. P. Anderson, A. L. Yeats, S. J. Whiteley, J. Niklas, O. G. Poluektov, F. J. Heremans, and D. D. Awschalom, Optical charge state control of spin defects in 4H-SiC, *Nature Communications* **8**, 1876 (2017).
- [14] Q. Li, J.-F. Wang, F.-F. Yan, J.-Y. Zhou, H.-F. Wang, H. Liu, L.-P. Guo, X. Zhou, A. Gali, Z.-H. Liu, Z.-Q. Wang, K. Sun, G.-P. Guo, J.-S. Tang, H. Li, L.-X. You, J.-S. Xu, C.-F. Li, and G.-C. Guo, Room-temperature coherent manipulation of single-spin qubits in silicon carbide with a high readout contrast, *National Science Review* **9**, nwab122 (2022).
- [15] Z.-X. He, J.-Y. Zhou, Q. Li, W.-X. Lin, R.-J. Liang, J.-F. Wang, X.-L. Wen, Z.-H. Hao, W. Liu, S. Ren, H. Li, L.-X. You, R.-J. Zhang, F. Zhang, J.-S. Tang, J.-S. Xu, C.-F. Li, and G.-C. Guo, Robust single modified divacancy color centers in 4H-SiC under resonant excitation, *Nature Communications* **15**, 10146 (2024).
- [16] F.-F. Yan, J.-F. Wang, Q. Li, Z.-D. Cheng, J.-M. Cui, W.-Z. Liu, J.-S. Xu, C.-F. Li, and G.-C. Guo, Coherent Control of Defect Spins in Silicon Carbide above 550 K, *Physical Review Applied* **10**, 044042 (2018).
- [17] H. Hu, G. Bian, A. Yi, C. Jiang, J. Tan, Q. Luo, B. Liang, Z. Liu, X. Nie, D. Lu, S. Xiao, X. Ou, A. Gali, Y. Zhou, and Q. Song, Strain-Enhanced Spin Readout Contrast in Silicon Carbide Membranes, *Physical Review Letters* **135**, 110601 (2025).
- [18] D. D. Awschalom, R. Hanson, J. Wrachtrup, and B. B. Zhou, Quantum technologies with optically interfaced solid-state spins, *Nature Photonics* **12**, 516 (2018).
- [19] See Supplemental Material at [URL] for additional figures and tables.
- [20] V. Ivády, J. Davidsson, N. Deegan, A. L. Falk, P. V. Klimov, S. J. Whiteley, S. O. Hruszkewycz, M. V. Holt, F. J. Heremans, N. T. Son, D. D. Awschalom, I. A. Abrikosov, and A. Gali, Stabilization of point-defect spin qubits by quantum wells, *Nature Communications* **10**, 5607 (2019).
- [21] N. T. Son, C. P. Anderson, A. Bourassa, K. C. Miao, C. Babin, M. Widmann, M. Niethammer, J. Ul Hassan, N. Morioka, I. G. Ivanov, F. Kaiser, J. Wrachtrup, and D. D. Awschalom, Developing silicon carbide for quantum spintronics, *Applied Physics Letters* **116**, 190501 (2020).
- [22] S. Castelletto, Silicon carbide single-photon sources: Challenges and prospects, *Materials for Quantum Technology* **1**, 023001 (2021).
- [23] S. Castelletto, A. Peruzzo, C. Bonato, B. C. Johnson, M. Radulaski, H. Ou, F. Kaiser, and J. Wrachtrup, Silicon Carbide Photonics Bridging Quantum Technology, *ACS Photonics* **9**, 1434 (2022).
- [24] G. Zhang, Y. Cheng, J.-P. Chou, and A. Gali, Material platforms for defect qubits and single-photon emitters, *Applied Physics Reviews* **7**, 031308 (2020).
- [25] N. T. Son, D. Shafizadeh, T. Ohshima, and I. G.

- Ivanov, Modified divacancies in 4H-SiC, *Journal of Applied Physics* **132**, 025703 (2022).
- [26] E. Vuillermet, N. Bercu, F. Etienne, and M. Lazar, Cathodoluminescence Characterization of Point Defects Generated through Ion Implantations in 4H-SiC, *Coatings* **13**, 992 (2023).
- [27] D. Shafizadeh, N. T. Son, I. A. Abrikosov, and I. G. Ivanov, Evolution of the optically detected magnetic resonance spectra of divacancies in 4H-SiC from liquid-helium to room temperature, *Physical Review B* **111**, 165201.
- [28] J. Li, H. Qi, F. Zhou, Y. Song, N. Xu, B. Hong, H. Chen, Y. Dong, and X. Wang, (2025), [arXiv:2503.22270 \[cond-mat\]](https://arxiv.org/abs/2503.22270).
- [29] R. Bai, D. Liu, S. Chen, and Y.-N. Wu, Origin of the unidentified color centers in 4H-SiC from first principles, *Physical Review B* **111**, 014106 (2025).
- [30] Q. Li, J.-F. Wang, F.-F. Yan, Z.-D. Cheng, Z.-H. Liu, K. Zhou, L.-P. Guo, X. Zhou, W.-P. Zhang, X.-X. Wang, W. Huang, J.-S. Xu, C.-F. Li, and G.-C. Guo, Nanoscale depth control of implanted shallow silicon vacancies in silicon carbide, *Nanoscale* **11**, 20554 (2019).
- [31] G. Feng, J. Suda, and T. Kimoto, Characterization of stacking faults in 4H-SiC epilayers by room-temperature microphotoluminescence mapping, *Applied Physics Letters* **92**, 221906 (2008).
- [32] T. Dalibor, H. Trageser, G. Pensl, T. Kimoto, H. Matsunami, D. Nizhner, O. Shigiltchhoff, and W. J. Choyke, Oxygen in silicon carbide: Shallow donors and deep acceptors, *Materials Science and Engineering: B* **61–62**, 454 (1999).
- [33] O. Klettke, G. Pensl, T. Kimoto, and H. Matsunami, Oxygen-Related Defect Centers Observed in 4H/6H-SiC Epitaxial Layers Grown under CO₂ Ambient, *Materials Science Forum* **353–356**, 459 (2001).
- [34] A. L. Falk, P. V. Klimov, B. B. Buckley, V. Ivády, I. A. Abrikosov, G. Calusine, W. F. Koehl, Á. Gali, and D. D. Awschalom, Electrically and Mechanically Tunable Electron Spins in Silicon Carbide Color Centers, *Physical Review Letters* **112**, 187601 (2014).
- [35] F. Dolde, H. Fedder, M. W. Doherty, T. Nöbauer, F. Rempp, G. Balasubramanian, T. Wolf, F. Reinhard, L. C. L. Hollenberg, F. Jelezko, and J. Wrachtrup, Electric-field sensing using single diamond spins, *Nature Physics* **7**, 459 (2011).
- [36] M. W. Doherty, F. Dolde, H. Fedder, F. Jelezko, J. Wrachtrup, N. B. Manson, and L. C. L. Hollenberg, Theory of the ground-state spin of the NV⁻ center in diamond, *Physical Review B* **85**, 205203 (2012).
- [37] G. Kresse and J. Hafner, Ab initio molecular dynamics for liquid metals, *Physical Review B* **47**, 558 (1993).
- [38] G. Kresse and J. Hafner, Ab initio molecular-dynamics simulation of the liquid-metal–amorphous-semiconductor transition in germanium, *Physical Review B* **49**, 14251 (1994).
- [39] P. E. Blöchl, Projector augmented-wave method, *Physical Review B* **50**, 17953 (1994).
- [40] J. P. Perdew, A. Ruzsinszky, G. I. Csonka, O. A. Vydrov, G. E. Scuseria, L. A. Constantin, X. Zhou, and K. Burke, Restoring the density-gradient expansion for exchange in solids and surfaces, *Physical Review Letters* **100**, 136406 (2008).
- [41] M. J. Rayson and P. R. Briddon, First principles method for the calculation of zero-field splitting tensors in periodic systems, *Physical Review B* **77**, 035119 (2008).
- [42] O. V. Yazyev, I. Tavernelli, L. Helm, and U. Röthlisberger, Core spin-polarization correction in pseudopotential-based electronic structure calculations, *Physical Review B* **71**, 115110 (2005).
- [43] A. V. Krukau, O. A. Vydrov, A. F. Izmaylov, and G. E. Scuseria, Influence of the exchange screening parameter on the performance of screened hybrid functionals, *The Journal of Chemical Physics* **125**, 224106 (2006).

Supplementary Material to “ Atomic structure of the PL5 defect in silicon carbide revealed by single-spin spectroscopy and oxygen implantation ”

CONTENTS

S1. Correlation Mapping of Stacking Fault and PL5/PL6	2
S1.1. Sample	2
S1.2. Identification and Localization of PL5 and PL6 Centers	2
S1.3. Stacking-Fault Characterization by Photoluminescence Spectroscopy	4
S1.4. Alignment of Confocal and Stacking-Fault Images	5
S2. Spatial Mapping of PL5 and PL6 Centers in Oxygen-Implanted Samples	6
S3. Orientation of PL5 Zero Field Splitting	7
S3.1. Orientation of axially symmetric spin splitting D	7
S3.2. Orientation of transverse anisotropy splitting E	8
S4. Nearest ^{13}C coupling	10
S5. Hyperfine Measurement	11
S5.1. Method	11
S5.2. Hyperfine Statistics	13
S5.3. Extent of the γB_z Deviation in Hyperfine Statistics	14
S6. Evaluate the Accuracy of Helmholtz’s Magnetic Field Setting	16
S7. <i>Ab Initio</i> Calculation of VVA Model	18
S8. Impact of Core Polarization on Hyperfine Coupling	20
References	21

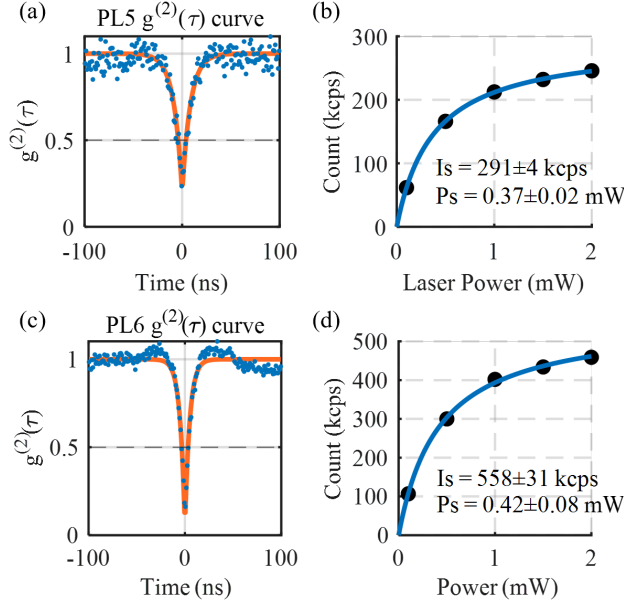


FIG. S1. (a) $g^2(\tau)$ measurement of single PL5. Clearly the anti-bunching $g^2(0) < 0.5$ shows it's a single optical emitter. (b) Saturation behavior of the PL of single PL5. The solid line was given by fitting $I(P) = I_s \cdot P / (P + P_s)$. (c) $g^2(\tau)$ measurement of single PL6. (d) Saturation behavior of the PL of single PL6. The solid line was given by fitting $I(P) = I_s \cdot P / (P + P_s)$.

S1. CORRELATION MAPPING OF STACKING FAULT AND PL5/PL6

S1.1. Sample

Sample for correlation mapping of stacking fault and PL5/6 were diced from a wafer consisting of a 12.5- μm -thick intrinsic epitaxial layer of single-crystal 4H-SiC grown on a 4° off-axis N-type 4H-SiC substrate. Patterns were created in the epitaxial layer surface by laser ablation for repositioning. Then the Sample was implanted with 15-keV $^{14}\text{N}^+$ at a dose of approximately $1 \times 10^{11} \text{ cm}^{-2}$. After Implantation, the sample was annealed in a furnace at 1000 $^\circ\text{C}$ for 30 minutes in a vacuum environment.

S1.2. Identification and Localization of PL5 and PL6 Centers

The locations of PL5 and PL6 centers were determined by first identifying all luminescent spots within the sample area and then screening for the specific spectroscopic signatures of PL5 and PL6.

A confocal image of the sample region was acquired under excitation with a circularly polarized 914 nm laser (3 mW), as shown in Fig. S2(a). A magnified view [Fig. S2(b)] reveals

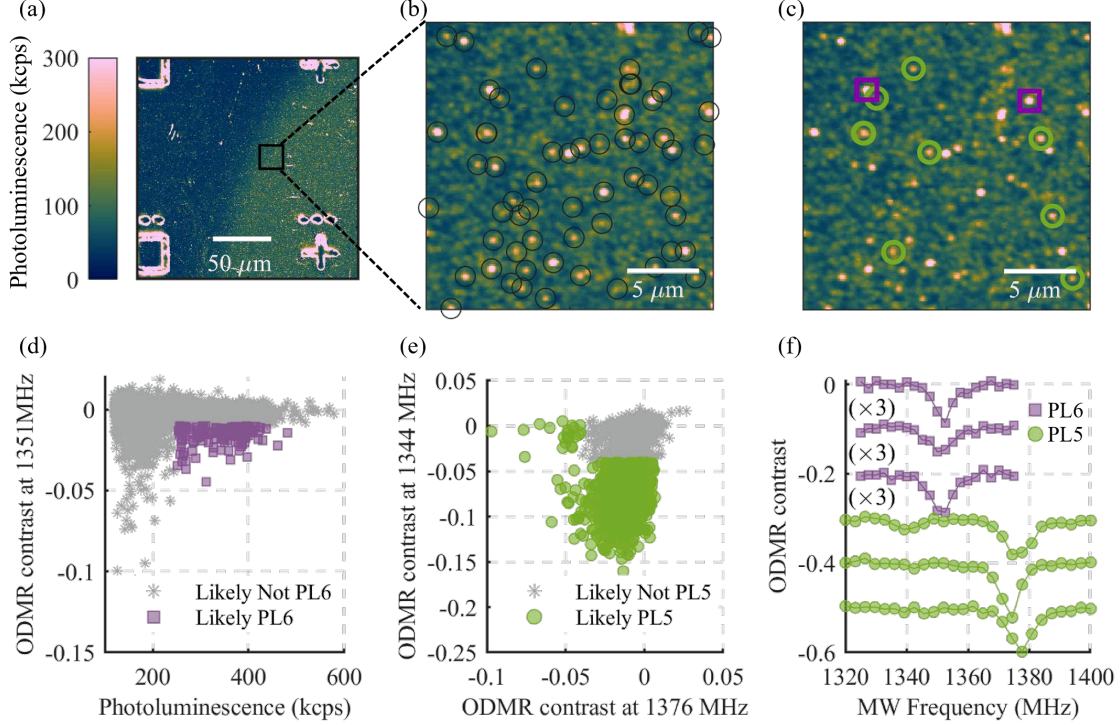


FIG. S2. (a) Confocal image of the sample under 914 nm circularly polarized excitation (3 mW). (b) Magnified view of the region indicated in (a); spots exceeding 100 kcps are circled in black. (c) The same region as in (b), with confirmed PL5 centers circled in green and PL6 centers marked with purple squares. (d) Selection of candidate PL6 centers based on photon count > 250 kcps and ODMR contrast at 1351 MHz < -0.02 . (e) Selection of candidate PL5 centers using ODMR contrast thresholds at 1344 MHz or 1376 MHz < -0.04 . (f) Representative zero-field ODMR spectra of randomly chosen PL5 and PL6 centers from the final dataset.

numerous bright spots. Based on the saturation count rates of individual PL5 (180–300 kcps) and PL6 (400–560 kcps) under 0.4–0.8 mW excitation (see Fig. S1), a threshold of 100 kcps was adopted for initial spot selection.

At zero magnetic field, PL6 exhibits an ODMR resonance near 1351 MHz, while PL5 shows two resonances near 1344 and 1376 MHz [1]. These frequencies were used to distinguish PL5 and PL6 from the general pool of luminescent spots. Candidate PL6 centers were selected by requiring a photon count > 250 kcps and an ODMR contrast at 1351 MHz below -0.02 [Fig. S2(d)]. Similarly, spots whose contrast at either 1344 or 1376 MHz fell below -0.04 were flagged as candidate PL5 centers [Fig. S2(e)].

Full ODMR spectra were then acquired for all candidate spots, allowing a final manual classification into PL5 and PL6. To illustrate the reliability of the procedure, Fig. S2(f) displays spectra of three randomly chosen PL5 and PL6 centers from the final dataset, showing the characteristic resonances near 1376 MHz for PL5 and 1351 MHz for PL6. The

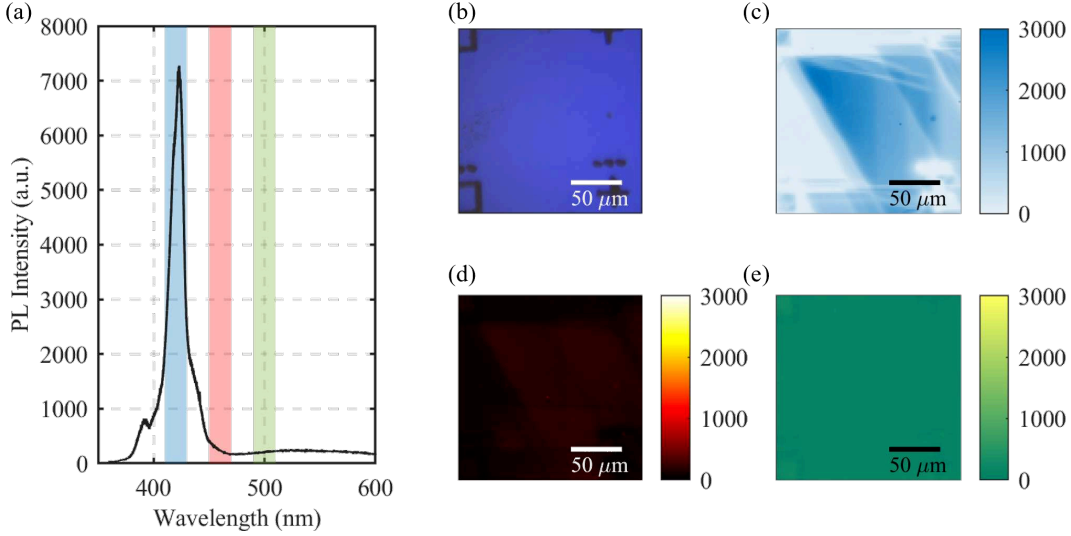


FIG. S3. (a) PL spectrum collected from the central region of (b). The peak around 420 nm originates from a stacking fault, while the weaker peak near 390 nm corresponds to the band-edge emission of 4H-SiC [2]. (b) Optical image of the sample. (c–e) Maps of the integrated PL intensity in the ranges 410–430 nm (c), 450–470 nm (d), and 490–510 nm (e), each associated with a distinct type of stacking fault.

outcome of the screening applied to the region in Fig. S2(b) is presented in Fig. S2(c).

We note that the 1344 MHz resonance of PL5 is not visible in the spectra of Fig. S2(f) due to the polarization of our microwave setup. This resonance requires linearly polarized excitation, whereas our radiating structure supplies a linear polarization nearly orthogonal to the required orientation. This was verified by applying a small magnetic field, which mixes the spin states and allows the resonance to be driven with circularly polarized microwaves, as confirmed on several PL5 centers.

S1.3. Stacking-Fault Characterization by Photoluminescence Spectroscopy

Room-temperature photoluminescence (PL) mapping was performed using a LabRAM HR Evolution (HORIBA) system with 325 nm laser excitation. Spectra were collected from 350 to 600 nm [Fig. S3(a)]. Three types of stacking faults in 4H-SiC are known to produce PL bands centered near 420, 455, and 500 nm, respectively [2]. To map their spatial distribution, we integrated the PL intensity over the intervals 410–430 nm [Fig. S3(c)], 450–470 nm [Fig. S3(d)], and 490–510 nm [Fig. S3(e)]. Only the stacking fault associated with the ~420 nm emission was detected in our sample.

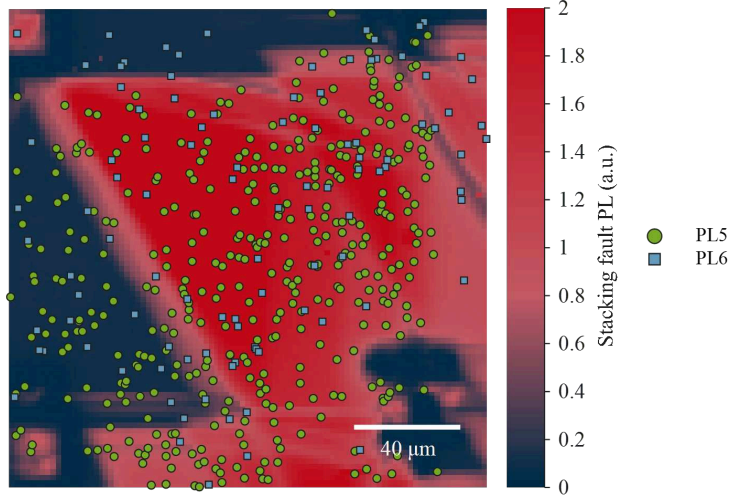


FIG. S4. Overlay of the confocal image of the stacking-fault edge region with the locations of identified PL5 (circles) and PL6 (squares) centers.

S1.4. Alignment of Confocal and Stacking-Fault Images

The confocal image of PL5/PL6 centers [Fig. S2(a)] and the stacking-fault PL map [Fig. S3(c)] were aligned using common markers ('+' and '·') present in both images. The alignment uncertainty is estimated to be $\sim 2 \mu\text{m}$. The resulting overlay is displayed in Fig. S4.

S2. SPATIAL MAPPING OF PL5 AND PL6 CENTERS IN OXYGEN-IMPLANTED SAMPLES

The spatial distribution of PL5 and PL6 centers in the oxygen-implanted sample was mapped using the pulse sequence depicted in Fig. S5(a). Reference photon counts (I_{ref}) were acquired under laser excitation alone, while signal counts (I_{signal}) were recorded with both laser excitation and resonant microwave irradiation. As shown in Fig. S5(b), the optically detected magnetic resonance contrast, calculated as $(I_{\text{signal}} - I_{\text{ref}})/I_{\text{ref}}$, varies with microwave frequency. PL5 exhibits a resonance at $f = 1374$ MHz, and PL6 resonates at $f = 1351$ MHz. Accordingly, at each pixel, the pulse sequence was applied at the respective resonant frequencies for PL5 and PL6, and both I_{ref} and I_{signal} were recorded. The resulting reference-count map is presented in Fig. S5(c). Maps of the normalized signal difference $I_{\text{signal}} - I_{\text{ref}}$ at the PL5 and PL6 resonance frequencies are displayed in Fig. S5(d) and (e), respectively. Based on these maps, the locations of PL5 and PL6 centers are indicated by circles and squares, respectively. The same procedure was applied to the nitrogen-implanted sample discussed in the main text. The scanned areas and the numbers of identified PL5 and PL6 centers for both samples are summarized in Table S1. All measurements were conducted under zero magnetic field.

TABLE S1: Number of ODMR-detected PL5 and PL6 centers in samples implanted with oxygen or nitrogen under identical conditions (15 keV, 10^{11} cm $^{-2}$, annealed at 1050 °C for 30 minutes).

	O implantation		N implantation	
Statistical area	10 $\mu\text{m} \times 10 \mu\text{m}$		10 $\mu\text{m} \times 10 \mu\text{m}$	
Counting rate of single spot (cps)	60–120 k		~25 k	
	PL5	PL6	PL5	PL6
Number of color centers	≥ 195	≥ 130	~18	~7
ODMR contrast	13%–18%	8%–14%	17%–20%	16%–20%
Generation Efficiency	$\geq 1.95\%$	$\geq 1.3\%$	0.18%	0.07%

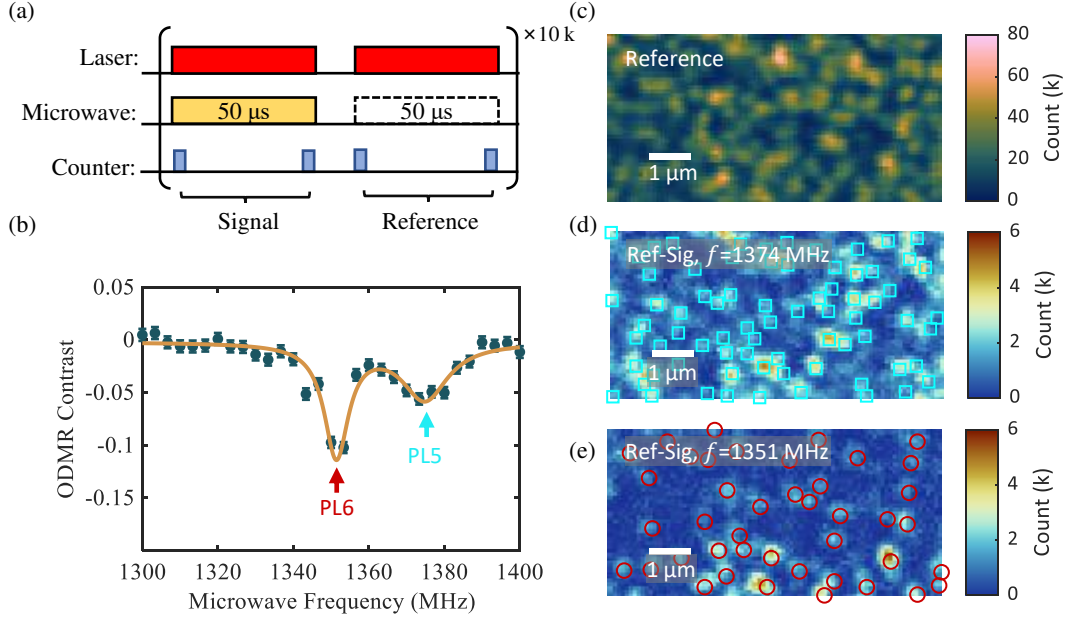


FIG. S5. (a) Pulse sequence used for ODMR-based spatial mapping. (b) Full zero-field ODMR spectrum acquired in the oxygen-implanted sample. (c) Reference photon-count map obtained with laser excitation only. (d) Difference map (reference – signal) measured at $f = 1374$ MHz, highlighting PL5 centers. (e) Difference map measured at $f = 1351$ MHz, highlighting PL6 centers.

S3. ORIENTATION OF PL5 ZERO FIELD SPLITTING

S3.1. Orientation of axially symmetric spin splitting D

In the main text, we have shown that PL5 exhibits six distinct orientations of the zero-field splitting parameter D , labeled D1 through D6. To determine these orientations accurately, we selected one representative color center for each of the six directions for further experimental characterization.

For each center, the approximate orientation was initially known, and this direction was used to define the z -axis of a local reference frame—referred to as the *estimation coordinate system*—as illustrated in Fig. S6(a). A magnetic field \mathbf{B} , expressed in spherical coordinates $(B, \theta_B^E, \phi_B^E)$ within this estimation frame, was applied using a three-axis Helmholtz coil. Let the orientation of the D tensor of a given color center be represented in the same estimation coordinates as $(1, \theta_{CC}^E, \phi_{CC}^E)$. The resulting ODMR splitting can then be described by

$$\text{Splitting} = 2\gamma B (\cos \theta_B^E \cos \theta_{CC}^E + \sin \theta_B^E \sin \theta_{CC}^E \cos (\phi_B^E - \phi_{CC}^E)) \quad (\text{S1})$$

By recording the splitting under various magnetic field orientations, we can fit the data

using Eq. (S1) to extract the parameters γB , θ_{CC}^E , and ϕ_{CC}^E .

Label	γB (MHz)	θ^{HC} (deg)	ϕ^{HC} (deg)
PL5(D1)	72.19±0.08	108.4±0.5	89.2±0.5
PL5(D2)	71.18±0.04	111.7±0.3	28.1±0.3
PL5(D3)	71.26±0.04	111.3±0.3	-32.4±0.3
PL5(D4)	70.55±0.08	107.6±0.6	-93.8±0.6
PL5(D5)	71.16±0.08	104.6±0.5	-153.9±0.5
PL5(D6)	73.01±0.05	105.0±0.4	148.8±0.4
PL6(C-axis)	137.87±0.05	4.7±0.2	-5±3

TABLE S2: Direction Measurement Eq. (S1) fitting results of different PL5-6 color centers. Results are given in Helmholtz Coil(HC) coordinate. We applied B=25 Gauss Magnetic field for PL5 and B=50 Gauss for PL6.

In practice, we fixed the field magnitude at $B = 25$ G and scanned the field direction around the initially estimated axis, as depicted in Fig. S6(a). For the D2 center, the measured ODMR splittings across different field orientations are shown in Fig. S6(b) and (c). The fitted orientation for this center is $\theta_{\text{D2}}^E = 2.8 \pm 0.2^\circ$ and $\phi_{\text{D2}}^E = 86 \pm 3^\circ$ in the estimation coordinate system.

Because each color center was analyzed in its own local estimation frame, we transformed all resulting orientations into a common reference frame—the *Helmholtz coil (HC) coordinate system*—for consistent comparison. The complete set of fitted orientations for PL5 (D1–D6) is summarized in Table S2.

S3.2. Orientation of transverse anisotropy splitting E

We characterized the transverse zero-field splitting parameter E for six individual PL5 centers, each exhibiting a distinct orientation (labeled D1 through D6). For each center, a coordinate system was carefully constructed such that the z -axis aligns with the orientation of D , and the x -axis lies in the plane formed by the z -axis and the $[0001]$ crystal direction. A magnetic field \mathbf{B} was applied perpendicular to the z -axis ($\mathbf{B} \perp \hat{z}$). Within this coordinate

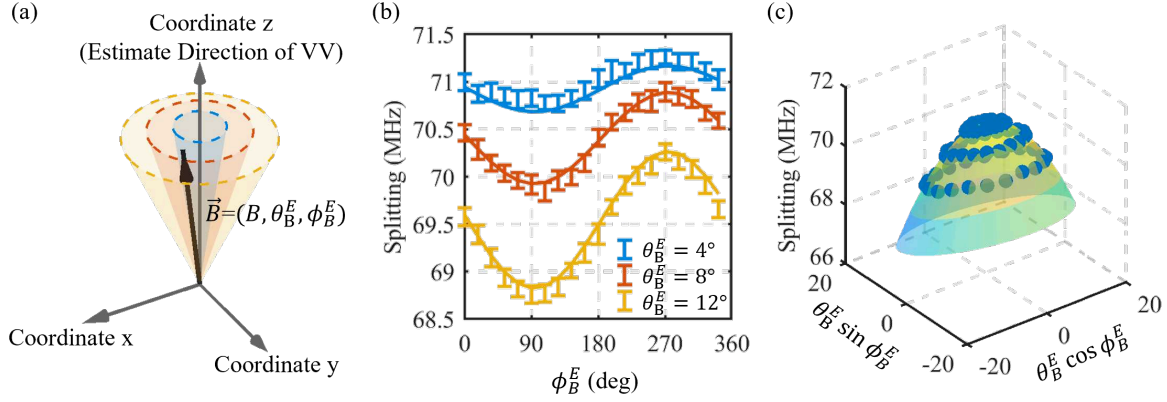


FIG. S6. (a) Illustration of the direction measurement. In the experiment, we fixed the amplitude of \vec{B} to be of $B = 25$ Gauss and let it scan in the spherical crown. For each magnetic field, we test the ODMR peak splitting. (b) ODMR peak splitting as a function of the direction (θ_B^E, ϕ_B^E) of the applied magnetic field. The solid lines represent the results provided by the fitting. (c) ODMR peak splitting as a function of the direction (θ_B^E, ϕ_B^E) of the applied magnetic field. The surface represents the results obtained from the fitting. Fitting gives out the direction of D1 $\theta_{D2}^E = 2.8 \pm 0.2$ deg and $\phi_{D2}^E = 86 \pm 3$ deg.

TABLE S3: Fitting Results of direction for transverse anisotropy splitting E .

PL5 Orientation	D2	D1	D6	D5	D4	D3
φ_E ($^\circ$)	186.8 ± 6.6	207.2 ± 10.4	182.2 ± 3.5	183.7 ± 6.0	178.2 ± 6.7	184.6 ± 5.1

frame, the effective spin Hamiltonian for the PL5 center can be written as

$$H/h = \frac{1}{\hbar^2} \left[D\hat{S}_z^2 - E_x(S_x^2 - S_y^2) + E_y(S_x S_y + S_y S_x) + \gamma\hbar(B_x S_x + B_y S_y) \right], \quad (\text{S2})$$

and the two magnetic dipole transition frequencies are given by [3, 4]

$$f_{\pm} \approx D + 3\eta \pm \left[E - 2\eta \sin \theta \cos(2\varphi_B + \varphi_E) + \eta^2 \right]^{1/2}, \quad (\text{S3})$$

where $\eta = B_{\perp}^2/(2D)$, $B_{\perp} = \sqrt{B_x^2 + B_y^2}$, $E = \sqrt{E_x^2 + E_y^2}$, and φ_B and φ_E denote the azimuthal angles of the in-plane magnetic field and the transverse anisotropy vector (E_x, E_y) , respectively.

Experimentally, the in-plane field magnitude was fixed at $B_{\perp} = 25$ G, and the frequency f_+ was recorded as a function of the in-plane field angle φ_B . The results for all six PL5 centers are presented in Fig. S7. Solid lines in the figure correspond to fits using Eq. (S3), and the extracted parameters are summarized in Table S3. Some deviations in the measurement results (like Fig. S7(b)) may be attributed to systematic errors and the instability of certain color centers.

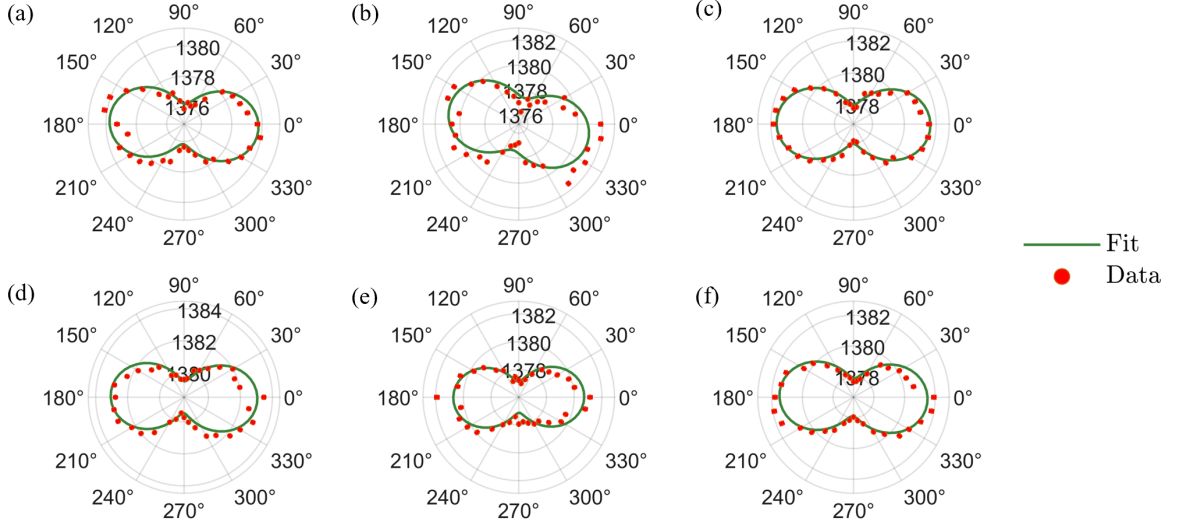


FIG. S7. (a)~(f) Stress field measurements on six PL5 color centers in different D orientations (from (a) to (f) corresponding to D2, D1, D6, D5, D4, D3). The angle of the polar plot denotes the azimuth angle φ_B of the magnetic field. The amplitude of the polar plot denotes magnetic transition f_+ . Red points represent the measured peak positions, while green lines show the fitting results.

S4. NEAREST ^{13}C COUPLING

In the experiment, the nuclear spin type (whether C_{Ia} or C_{Ib}) can be identified from the ODMR spectrum obtained under a non-aligned magnetic field [see Fig. S8(a)]. We measured the hyperfine splittings δ_{12} and δ_{34} under an axial magnetic field ranging from 90 to 200 G. As shown in Fig. S8(b), δ_{12} and δ_{34} exhibit a slight difference, which originates from the strong hyperfine coupling.

While the individual splittings δ_{12} and δ_{34} are sensitive to both the magnitude and alignment accuracy of the applied field, their mean value $\delta = (\delta_{12} + \delta_{34})/2$ remains largely unaffected by these experimental variations. Fig. S8(c) plots δ for both C_{Ia} and C_{Ib} nuclear-spin types; the corresponding numerical values are listed in Table S4.

PL5 Direction	Nuclear Location	B (Gauss)	δ_{12} (MHz)	δ_{34} (MHz)
D5	Unclassified	91	54.4 ± 1.3	53.7 ± 2.1
D5	C _{Ia}	91	54.2 ± 0.5	53 ± 0.8
D5	C _{Ib}	91	53.9 ± 0.4	54.6 ± 0.4
D2	C _{Ib}	185	55.3 ± 0.5	53.4 ± 0.4
D2	C _{Ia}	185	53.7 ± 0.3	53.7 ± 0.5
D4	C _{Ib}	185	54.0 ± 0.2	54.9 ± 0.2
D1	C _{Ia}	168	52.0 ± 0.4	54.6 ± 0.5
D1	C _{Ia}	168	54.3 ± 0.3	52.7 ± 0.3

TABLE S4: Measured splitting δ_{12} and δ_{34} of different PL5. The uncertainty is given at a 95% confidence level.

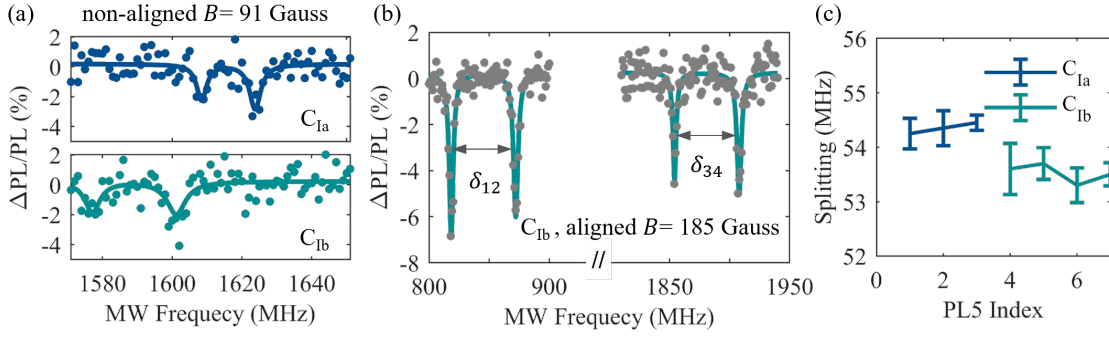


FIG. S8. (a) ODMR spectra of a D2-oriented PL5 center coupled to a C_{Ia} (top) and a C_{Ib} (bottom) nuclear spin, acquired with a magnetic field $B = 91$ G applied along the D5 direction. (b) ODMR spectrum of a PL5 center coupled to a C_{Ia} nuclear spin, measured under $B = 185$ G. (c) Mean hyperfine splitting $\delta = (\delta_{12} + \delta_{34})/2$ for C_{Ia} and C_{Ib} nuclear spins.

S5. HYPERFINE MEASUREMENT

S5.1. Method

When a single nuclear spin couples to the PL5 center, the Hamiltonian of the PL5 ground state can be written as [3, 5]

$$\begin{aligned}
 H/h = \frac{1}{\hbar^2} & \left(D\hat{S}_z^2 - E_x(S_x^2 - S_y^2) + E_y(S_xS_y + S_yS_x) \right. \\
 & \left. + \gamma\hbar\mathbf{B} \cdot \hat{\mathbf{S}} + \hat{\mathbf{S}} \cdot \mathbf{A} \cdot \hat{\mathbf{I}} + \gamma_C\hbar\mathbf{B} \cdot \hat{\mathbf{I}} \right), \tag{S4}
 \end{aligned}$$

where D is the longitudinal zero-field splitting, E_x and E_y are the transverse zero-field splitting components, γ denotes the electron gyromagnetic ratio, $\hat{\mathbf{S}}$ and $\hat{\mathbf{I}}$ are the electron

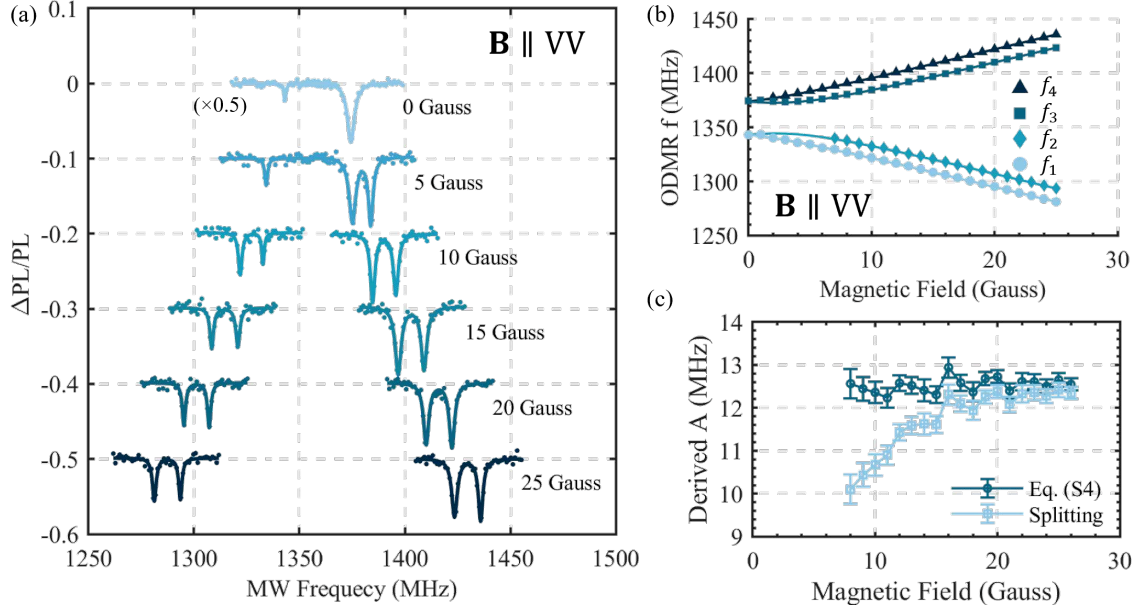


FIG. S9. (a) ODMR spectra of a selected PL5 center under different magnetic fields. The zero-field spectrum is scaled down by a factor of 2 for clarity. (b) Measured transition frequencies $f_{1,2,3,4}$ (points) as a function of magnetic field. Solid curves are calculated from Eq. (S5) with $D = 1358.5$ MHz, $E = 14.1$ MHz, and $A = 12.5$ MHz. (c) Hyperfine component A_z derived via Eq. (S6) (dark green) and via the direct splitting $A_z^{(\text{split})}$ (light blue).

and nuclear spin operators, respectively, \mathbf{A} is the hyperfine tensor for a spin-1/2 nucleus, and \mathbf{B} is the external magnetic field. The nuclear Zeeman term is neglected in the following. We adopt a coordinate system in which the z -axis coincides with the orientation of the PL5 center, and the x -axis lies in the symmetry plane of the 4H-SiC crystal and is perpendicular to z .

In the regime $\mathbf{B}, \mathbf{A} \ll D$, first-order perturbation theory yields four transition frequencies

$$f \approx D \pm \sqrt{(\gamma B_z \pm A_z/2)^2 + E^2}, \quad (\text{S5})$$

with $E = \sqrt{E_x^2 + E_y^2}$ and $A_z = |\hat{z} \cdot \mathbf{A}|$. These frequencies are labeled $f_{1,2,3,4}$ in increasing order.

As illustrated in Fig. S9(a), a single PL5 coupled to a single nuclear spin shows no resolvable hyperfine splitting at zero magnetic field because of the transverse zero-field term. When a finite magnetic field is applied, the splitting appears and eventually saturates. Experimentally measured transition frequencies as a function of field are presented in Fig. S9(b); they are well described by Eq. (S5) with appropriate parameters.

In the main text, the hyperfine component A_z is extracted via

$$A_z = \frac{(f_4 - f_1)^2 - (f_2 - f_3)^2}{8\gamma B_z}, \quad (\text{S6})$$

which follows directly from Eq. (S5). Here $f_{1,2,3,4}$ are obtained from the ODMR spectra, and γB_z must be determined independently. We adopt $\gamma = 2.8$ MHz/G and assume that the magnetic field is well aligned with the PL5 axis, so that $B_z \approx B$, where B is the nominal field set by the Helmholtz coils. The small discrepancy between the nominal and actual field (discussed in later sections) is negligible for the hyperfine determination. To verify this assumption, we fit the quantity $(f_4 - f_1)^2 + (f_3 - f_2)^2$ to $8aB^2 + b$, yielding $\gamma B_z = \sqrt{a} B$. The fit gives $\gamma B_z = 2.786(4)$ MHz/G $\times B$, in excellent agreement with the assumed value.

Fig. S9(c) compares the hyperfine component A_z computed from Eq. (S6) with the simple hyperfine splitting $A_z^{(\text{split})} = [(f_2 - f_1) - (f_4 - f_3)]/2$, using the same data as in Fig. S9(b). Eq. (S6) clearly provides a more consistent result across different magnetic fields.

S5.2. Hyperfine Statistics

To survey the hyperfine properties of PL5 centers, we performed ODMR spectroscopy on 473 individual PL5 centers under an off-axis magnetic field of 15 G. Representative spectra are displayed in Fig. S10(a). According to the number of resolved resonance peaks, we classified the centers into three categories: (1) two peaks (no strong hyperfine coupling), (2) four peaks (coupling to a single nuclear spin), and (3) multiple peaks (coupling to several nuclear spins). The classification results are summarized in Table S5. Note that centers with weak hyperfine coupling may be misclassified as “no coupling” if the splitting is obscured by line broadening. To assess this possibility, we analyzed the distribution of ODMR linewidths for the two-peak centers, as shown in Fig. S10(b).

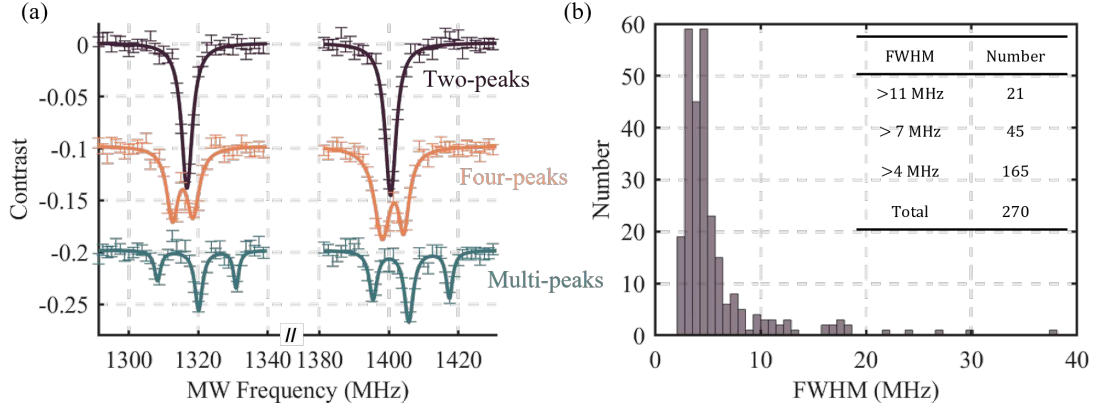


FIG. S10. (a) Representative ODMR spectra acquired under a 15 G off-axis magnetic field. (b) Distribution of the full-width-at-half-maximum (FWHM) for the two-peak centers shown in (a).

TABLE S5: Classification of PL5 ODMR spectra measured under $B = 15$ G.

Coupling type	Number	Percentage
No nuclear spin	276	58.4%
Single nuclear spin	139	29.4%
Multiple nuclear spins	34	7.2%
Unresolved	24	5.1%
Total	473	100%

The six possible orientations of PL5 form an angle of about 71° with the crystal c -axis. For the hyperfine survey, we divided them into three groups (illustrated in Fig. S11(a-c)). For each group we aimed to align the magnetic field so that its angle relative to every center in the group was approximately equal. In practice, small misalignments were unavoidable; their effect is quantified in the next subsection. The values of γB_z used for the hyperfine analysis in each group are listed in Table S6.

S5.3. Extent of the γB_z Deviation in Hyperfine Statistics

For the hyperfine survey we applied a field $B = 15$ G at an intended angle of 19.5° relative to the PL5 axis, giving an expected $\gamma B_z \approx 2.8 \times 15 \times \cos 19.5^\circ = 39.6$ MHz. Deviations from this value arise from two main sources: (1) the finite setting accuracy of the Helmholtz coils, which introduces an uncertainty of about 1 MHz at 15 G (see Section S6); and (2) small

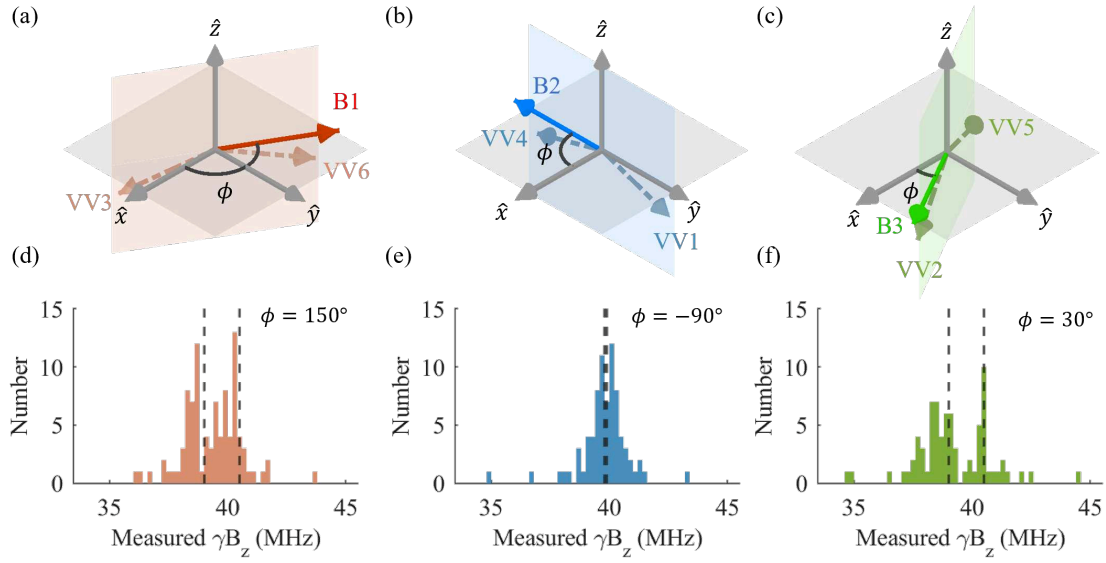


FIG. S11. (a–c) Schematic of the magnetic-field alignment for the three orientation groups defined in Table S6. (d–f) Distributions of γB_z extracted from two-peak centers via Eq. (S7). Dashed lines mark the γB_z values in Table S6.

angular misalignments between the intended field direction and the actual PL5 orientation, quantified in Table S6. For each group we mitigate the latter by using the average γB_z of the two orientations in that group. As seen from the table, the angular contribution to the uncertainty is also about 1 MHz. Combining both sources, we estimate the total uncertainty in γB_z to be ~ 1 MHz for all groups.

We cross-checked this estimate by analyzing the PL5 color centers identified as no strong hyperfine coupling in the hyperfine survey (Table S5). For a PL5 without hyperfine coupling, the axial field component can be obtained from the two observed transition frequencies via

$$\gamma B_z = \sqrt{[(f_2 - f_1)/2]^2 - E^2} \quad (\text{S7})$$

where $f_{1,2} = D \mp \sqrt{(\gamma B_z)^2 + E^2}$. The distributions of γB_z obtained from Eq. (S7) for the three groups are shown in Fig. S11(d–f). Dashed lines indicate the γB_z values in Table S6; the agreement is good apart from a few outliers.

TABLE S6: Magnetic-field components γB_z for the three orientation groups. The PL5 orientations $\theta_{CC}^{\text{HC}}, \phi_{CC}^{\text{HC}}$ are taken from [Table S2](#). The gyromagnetic ratio is $\gamma = 2.8 \text{ MHz/G}$.

Field direction (HC coordinates)	PL5	θ_{CC} (deg)	ϕ_{CC} (deg)	γB_z (MHz)	γB_z (MHz) (average)
$\theta_B = 90^\circ$	D1	108.4 ± 0.5	89.2 ± 0.5	39.85	39.90
$\phi_B = -90^\circ$	D4	107.6 ± 0.6	-93.8 ± 0.6	39.95	
$\theta_B = 90^\circ$	D2	111.7 ± 0.3	28.1 ± 0.3	39.00	39.76
$\phi_B = 30^\circ$	D5	104.6 ± 0.5	-153.9 ± 0.5	40.55	
$\theta_B = 90^\circ$	D3	111.3 ± 0.3	-32.4 ± 0.3	39.10	39.83
$\phi_B = 150^\circ$	D6	105.0 ± 0.4	148.8 ± 0.4	40.56	

S6. EVALUATE THE ACCURACY OF HELMHOLTZ'S MAGNETIC FIELD SETTING

COLIY G93 gaussmeter was used for the calibration of the three-axis Helmholtz coils. Our three-axis Helmholtz coils are composed of three pairs of Helmholtz coils, namely X, Y, and Z coils. For each pair of coils, we set the magnetic field to be $\mathbf{B}_{\text{set}} = B_{\text{set}} \mathbf{n}_{\text{set}}$ and measure the actual magnetic field \mathbf{B}_{mea} . The deviation is given by $\mathbf{B}_d = \mathbf{B}_{\text{mea}} - \mathbf{B}_{\text{set}}$. We further divide \mathbf{B}_d as $\mathbf{B}_d = \mathbf{B}_{d\parallel} + \mathbf{B}_{d\perp}$ in which $\mathbf{B}_{d\parallel} // \mathbf{B}_{\text{set}}$ and $\mathbf{B}_{d\perp} \perp \mathbf{B}_{\text{set}}$. The measured deviation for $\mathbf{B}_{d\parallel}$ and $\mathbf{B}_{d\perp}$ are both ~ 1 Gauss which is mainly due to the magnetism of the objective ([Fig. S12](#)).

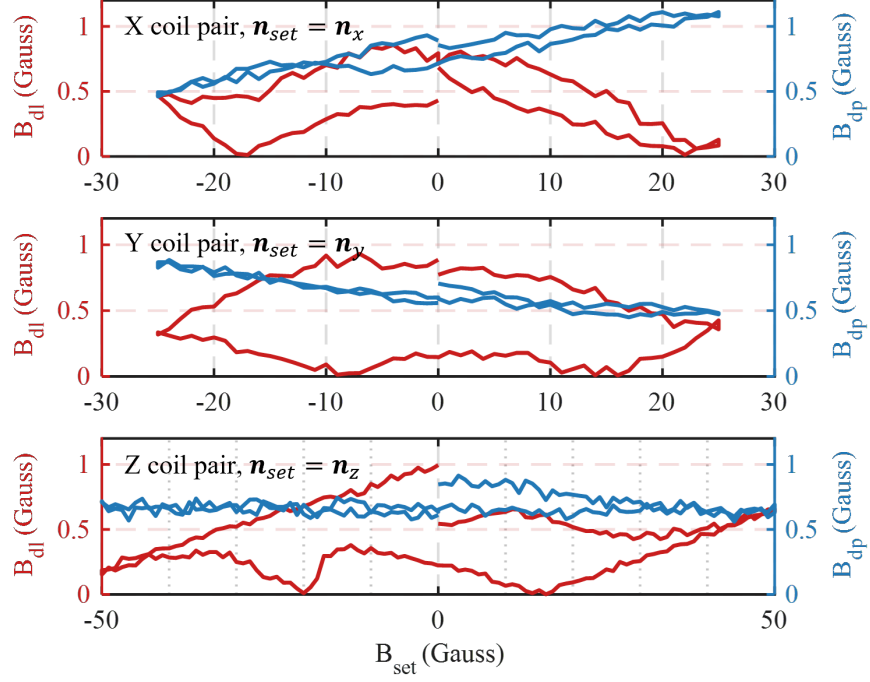


FIG. S12. Magnetic field deviations $\mathbf{B}_d = \mathbf{B}_{dl} + \mathbf{B}_{dp}$, measured as a function of the set field $\mathbf{B}_{set} = B_{set}\mathbf{n}_{set}$, where \mathbf{B}_{dl} is parallel to \mathbf{B}_{set} and \mathbf{B}_{dp} is perpendicular to \mathbf{B}_{set} . The field B_{set} was initially set to zero, then gradually increased, decreased to a negative value, and finally returned to zero. The primary cause of the deviation is the magnetism of the objective.

S7. AB INITIO CALCULATION OF VVA MODEL

The consideration of divacancy with nearby antisite (VVA) model was motivated by the possibility of $V_{\text{Si}} + V_{\text{C}}\text{C}_{\text{Si}} \rightarrow V_{\text{Si}}V_{\text{C}}\text{C}_{\text{Si}}$ process. At annealing temperature 900–1000 °C, V_{Si} becomes mobile in n-type conditions [6–9], enabling encounters with $V_{\text{C}}\text{C}_{\text{Si}}$ to form $V_{\text{Si}}V_{\text{C}}\text{C}_{\text{Si}}$. At appropriate Fermi level, V_{Si}^- and $V_{\text{C}}\text{C}_{\text{Si}}^+$ are respectively the most stable charge states [10], further promoting their pairing via Coulomb attraction.

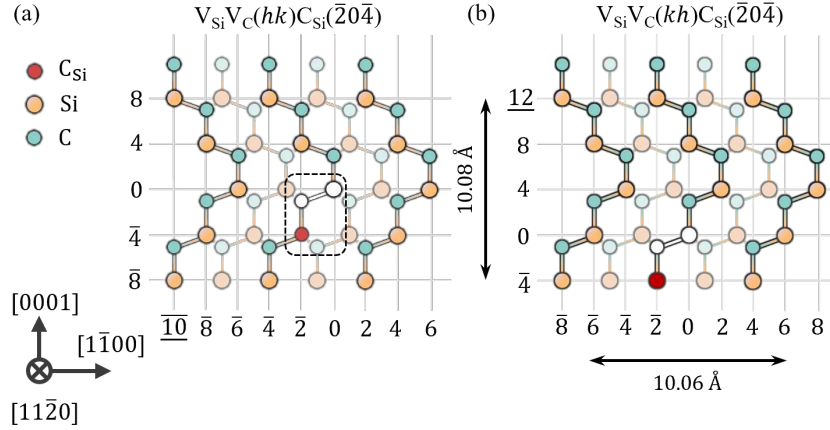


FIG. S13. (a-b) $V_{\text{Si}}V_{\text{C}}(hk)\text{C}_{\text{Si}}(\bar{2}0\bar{4})$ and $V_{\text{Si}}V_{\text{C}}(kh)\text{C}_{\text{Si}}(\bar{2}0\bar{4})$ configurations in 4H-SiC. The antisite atom location is labeled by ijk , corresponding to the crystallographic directions $[1\bar{1}00]$, $[11\bar{2}0]$, and $[0001]$. Taking the silicon vacancy in divacancy as the origin, these indices are proportional to the projection of the antisite location onto the $[1\bar{1}00]$, $[11\bar{2}0]$, and $[0001]$ axes.

Table S7 lists *ab initio* calculation results for several VVA configurations. Choosing the silicon vacancy in divacancy as the origin, the antisite atom location is labeled by ijk , which are proportional to the projection of the antisite location to the $[1\bar{1}00]$, $[11\bar{2}0]$, and $[0001]$ directions. For example, Fig. S13 illustrates the $V_{\text{Si}}V_{\text{C}}(hk)\text{C}_{\text{Si}}(\bar{2}0\bar{4})$ and $V_{\text{Si}}V_{\text{C}}(kh)\text{C}_{\text{Si}}(\bar{2}0\bar{4})$ configuration in 4H-SiC.

TABLE S7: Comparison of selected *ab initio* calculation results of VVA model with experimental properties of PL5.

Label	ZPL (eV)	D (MHz)	E_x (MHz)	$ E_y $ (MHz)	$\delta(C_{1a}) - \delta(C_{1b})$ (MHz)
(Exp.) PL5	1.189	1373	-16.5	<0.5	0.88
(Cal.) $V_{\text{Si}}V_{\text{C}}(hk)\text{C}_{\text{Si}}(\bar{2}0\bar{4})$	1.13	1527	5.8	<0.05	3.11

Within the computational uncertainty, the calculated properties of $V_{\text{Si}}V_{\text{C}}(hk)\text{C}_{\text{Si}}(\bar{2}0\bar{4})$ are consistent with the experimental observations of PL5. Our calculations further yield

minimum energy barriers of 3.15 eV for V_{Si} migration and 1.16 eV for the pairing reaction $V_{\text{Si}} + V_{\text{C}}C_{\text{Si}} \rightarrow V_{\text{Si}}V_{\text{C}}(hk)C_{\text{Si}}(\bar{2}0\bar{4})$, supporting the plausibility of this defect as a candidate for PL5.

Nevertheless, the VVA model struggles to account for the oxygen-implantation results, which show a marked increase in PL5 generation efficiency compared to nitrogen implantation. One could speculate that the formation of VVA ($V_{\text{Si}} + V_{\text{C}}C_{\text{Si}} \rightarrow V_{\text{Si}}V_{\text{C}}C_{\text{Si}}$) competes with divacancy formation ($V_{\text{Si}} + V_{\text{C}} \rightarrow V_{\text{Si}}V_{\text{C}}$). In this scenario, implanted oxygen might reduce the concentration of V_{C} via the reaction $O_{\text{i}} + V_{\text{C}} \rightarrow O_{\text{C}}$, thereby suppressing divacancy formation and indirectly enhancing VVA generation. However, such assumptions remain speculative and introduce considerable complexity compared to the more straightforward oxygen-vacancy (OV) model.

S8. IMPACT OF CORE POLARIZATION ON HYPERFINE COUPLING

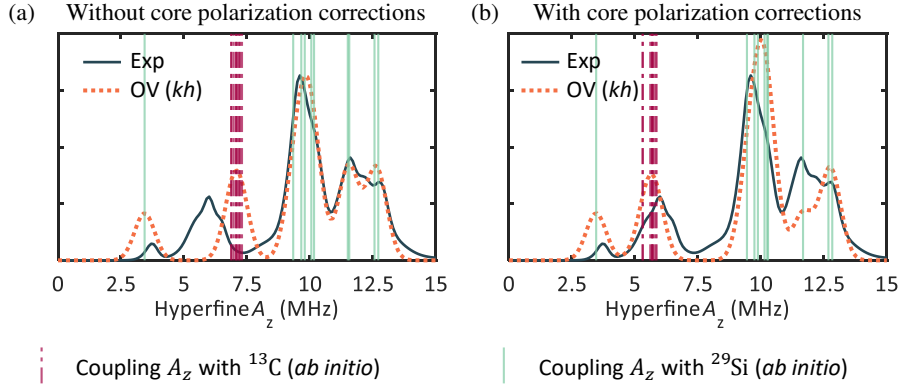


FIG. S14. Comparison of experimental (black solid curve) and simulated (orange dashed curve) A_z distributions. (a) Simulated hyperfine distribution without core polarization corrections. (b) Simulated hyperfine distribution with core polarization corrections included.

In the main text, we report the calculated hyperfine interactions for the $O_C V_{Si}(kh)$ defect structure, including core electronic contributions. To more comprehensively evaluate the impact of core electronic contributions and to compare with computational setups commonly adopted in prior studies—such as the approach used in our previous work [11]—we supplement here the corresponding results without core polarization corrections, which are shown in Fig. S14(a). The primary effect of core electronic contributions is reflected in measurable shifts in the peak positions at the ^{13}C nuclei, whereas the relative spectral line shapes and distributions are less affected. In the main text, we choose to present results that include core electronic contributions to provide the closest description to physical reality. The uncorrected results provided here serve as a reference for direct comparison with earlier theoretical studies that did not account for such effects—for instance, in discussions concerning structures with C_{3v} symmetry. The similarity of the conclusions under both computational schemes further strengthens the robustness of the main findings of this study. In summary, incorporating core electronic contributions improves our theoretical model, while the uncorrected results demonstrate that the hyperfine interaction characteristics of this defect structure remain stable within a certain range of computational details.

-
- [1] Q. Li, J.-F. Wang, F.-F. Yan, J.-Y. Zhou, H.-F. Wang, H. Liu, L.-P. Guo, X. Zhou, A. Gali, Z.-H. Liu, Z.-Q. Wang, K. Sun, G.-P. Guo, J.-S. Tang, H. Li, L.-X. You, J.-S. Xu, C.-F. Li, and G.-C. Guo, *National Science Review* **9**, nwab122 (2021).
- [2] G. Feng, J. Suda, and T. Kimoto, *Applied Physics Letters* **92**, 221906 (2008).
- [3] M. W. Doherty, F. Dolde, H. Fedder, F. Jelezko, J. Wrachtrup, N. B. Manson, and L. C. L. Hollenberg, *Physical Review B* **85**, 205203 (2012).
- [4] F. Dolde, H. Fedder, M. W. Doherty, T. Nöbauer, F. Rempp, G. Balasubramanian, T. Wolf, F. Reinhard, L. C. L. Hollenberg, F. Jelezko, and J. Wrachtrup, *Nature Physics* **7**, 459 (2011).
- [5] K. C. Miao, A. Bourassa, C. P. Anderson, S. J. Whiteley, A. L. Crook, S. L. Bayliss, G. Wolfowicz, G. Thiering, P. Udvarhelyi, V. Ivády, H. Abe, T. Ohshima, Á. Gali, and D. D. Awschalom, *Science Advances* **5**, eaay0527 (2019).
- [6] C. Zhang, F. Gygi, and G. Galli, *Nature Communications* **14**, 5985 (2023).
- [7] F. Fuchs, B. Stender, M. Trupke, D. Simin, J. Pflaum, V. Dyakonov, and G. V. Astakhov, *Nature Communications* **6**, 7578 (2015).
- [8] T. Kobayashi, M. Rühl, J. Lehmeier, L. K. S. Zimmermann, M. Krieger, and H. B. Weber, *Journal of Physics D: Applied Physics* **55**, 105303 (2021).
- [9] A. F. M. Almutairi, J. G. Partridge, C. Xu, I. S. Cole, and A. S. Holland, *Applied Physics Letters* **120**, 014003 (2022).
- [10] R. Karsthof, M. E. Bathen, A. Galeckas, and L. Vines, *Physical Review B* **102**, 184111 (2020).
- [11] X. Zhao, M. Liu, Y. Chen, Q. Zhang, and C.-K. Duan, *Physical Review Materials* **9**, 116204 (2025).